CONDENSED MATTER PHYSICS

Selective trapping of hexagonally warped topological surface states in a triangular quantum corral

Mu Chen[1,2], Ye-Ping Jiang[3]*, Junping Peng[1], Huimin Zhang[1], Cui-Zu Chang[1,4], Xiao Feng[1], Zhenguo Fu[5], Fawei Zheng[5], Ping Zhang[5], Lili Wang[1,6], Ke He[1,6], Xu-Cun Ma[1,6]*, Qi-Kun Xue[1,6,7]*

The surface of a three-dimensional topological insulator (TI) hosts two-dimensional massless Dirac fermions (DFs), the gapless and spin-helical nature of which leads to their high transmission through surface defects or potential barriers. Here, we report the behaviors of topological surface states (TSS) in a triangular quantum corral (TQC) which, unlike a circular corral, is supposed to be totally transparent for DFs. By real-space mapping of the electronic structure of TQCs, both the trapping and detrapping behaviors of the TSS are observed. The selection rules are found to be governed by the geometry and spin texture of the constant energy contour of TSS upon the strong hexagonal warping in Bi_2Te_3. Our work indicates the extended nature of TSS and elucidates the selection rules of the trapping of TSS in the presence of a complicated surface state structure, giving insights into the effective engineering of DFs in TIs.

INTRODUCTION

The existence of topological surface states (TSS), with their low-energy behavior described by the Dirac equation rather than the Schrödinger equation, is ensured by the twisted bulk band topology resulting from the strong spin-orbital coupling of the material (*1*, *2*). Unlike the massive electron systems having a forbidden gap, such as any trivial band insulator and even massive Dirac systems, the gapless Dirac fermion (DF) nature of TSS makes the potential barriers leaky (*3*). Furthermore, as long as time-reversal symmetry is respected, the backscattering of TSS is prohibited because of its helical nature (*3*–*5*), leading to the full transmission of normal incident electrons through potential barriers. This situation is more prominent for a family of three-dimensional (3D) topological insulators (TIs) (Bi_2Se_3, Bi_2Te_3, and Sb_2Te_3) (*6*–*9*), which have a single Dirac cone in the surface state structure and only one Fermi surface on the constant energy contour (CEC) within the bulk gap, further eliminating possible backscattering channels. Thus, the two fundamental properties of TSS, gaplessness and helical spin texture, may render any conventional quantum corral (*10*) highly leaky and complete trapping of TSS impossible, similar to the case of DFs in graphene (*11*).

For a 1D barrier on the TI surface, although reflection for normal incident electrons is forbidden, the reflection at oblique angles is possible, and even dominates the tunneling process at large incident angles, approaching one at grazing angles (*12*), which is governed by the spin texture of the CEC (*13*, *14*). This makes the quasi-bounding of TI surface states possible via whispering-gallery modes as observed in a circular graphene pn junction (*15*–*17*) or, in the case of antimony, by constructing a Fabry-Pérot resonator (*3*, *12*), the "infinity" of which along the 1D barriers helps to trap the TSS. However, antimony has a more complicated surface state structure (*18*), which facilitates backscattering and makes the trapping behavior of surface states more conventional. The abovementioned approaches both use the high reflection probability at near-grazing angles of DFs. Their intriguing attributes pique interest to construct different resonators, in which electrons can no longer keep bouncing at grazing angles, on TIs but with simple CECs.

Here, we successfully constructed such resonators as triangular quantum corrals (TQCs) on the surface of a 3D TI, Bi_2Te_3, which has a single Dirac cone and only one Fermi surface on the CEC in the surface state structure within the gap (*6*). Although the trapping of DFs by TQCs seems impossible because of the above argument, our experiments show well-defined interference patterns in some energy ranges of the TSS band. The trapping of Dirac electrons is found to be assisted by the hexagonal warping effect in the TSS, which in Bi_2Te_3 (*19*) is much stronger than that in Bi_2Se_3 (*20*). As shown below, the strong warping effect of TSS in Bi_2Te_3 yields energy-dependent trapping behaviors and selection rules of TSS in TQCs. Careful analysis of the quantum interference patterns of quasi-bound states yields the corresponding wave vectors of trapped TSS, through which two trapping mechanisms favoring momenta in different directions are uncovered.

RESULTS

MBE fabrication of TQCs and the observation of trapped TSS

Our TQCs are constructed by heteroepitaxially growing a Bi bilayer (BL) on the surface of the Bi_2Te_3 thin film (see Materials and Methods). The previous work (*21*) shows that at appropriate Bi coverages (typically 0.9 BL), Bi_2Te_3 vacancy islands surrounded by the Bi BL film can be formed. Taking an island with the side length L of ~35 nm, a close scrutiny uncovers quasi-equilateral triangular vacancy islands (Fig. 1A), bounded by $\langle\bar{1}01\rangle$-, $\langle1\bar{1}0\rangle$-, and $\langle01\bar{1}\rangle$-oriented steps of the Bi BL (*21*). The depth of the vacancy island height is ~4.8 Å and bias voltage independent. The defect-free atomic resolution image inside the TQC demonstrates that the Te-terminated Bi_2Te_3 (111) surface has a lattice spacing of ~4.4 Å, consistent with the bulk lattice constant (*22*). The orientations of the triangular sides of the vacancy island align with the $\bar{\Gamma}-\bar{K}$ directions of the Bi_2Te_3 surface Brillouin zone.

The Dirac energy of the pristine Bi_2Te_3 film locates at ~−170 meV (fig. S1) and is buried below the bulk valence band. Compared with pristine films, the dI/dV spectrum taken at the TQC center shows a downward shift of ~130 meV (blue curve in Fig. 1B), indicating the

[1]Department of Physics, Tsinghua University, Beijing 100084, China. [2]Beijing Institute of Aeronautical Materials, Beijing 100095, China. [3]Key Laboratory of Polar Materials and Devices (MOE), Department of Optoelectronics, East China Normal University, Shanghai 200241, China. [4]Department of Physics, Pennsylvania State University, University Park, PA 16802, USA. [5]Institute of Applied Physics and Computational Mathematics, Beijing 100088, China. [6]Collaborative Innovation Center of Quantum Matter, Beijing 100084, China. [7]Beijing Academy of Quantum Information Sciences, Beijing 100193, China.
*Corresponding author. Email: ypjiang@clpm.ecnu.edu.cn (Y.-P.J.); xucunma@mail.tsinghua.edu.cn (X.-C.M.); qkxue@mail.tsinghua.edu.cn (Q.-K.X.)

electron-doping effect of the Bi BL on the Bi_2Te_3 film (*21*). The Dirac energy of TSS in the uncovered region should be around −300 meV. The presence of a Bi BL changes the boundary condition of the Bi_2Te_3 film, and the Dirac energy is lifted to ~−210 meV. Therefore, there is a mismatch between the Dirac energies across the interface along $\bar{\Gamma}-\bar{K}$ directions between Bi_2Te_3 and Bi/Bi_2Te_3 regions, in addition to the potential barriers caused by the steps. TQCs are thus formed on the surface of Bi_2Te_3 films for further study of trapping behaviors of TSS, as discussed below.

We note that the peaks shown in the spectrum taken at the TQC center (Fig. 1B) reveal the occurrence of quantized states, which is against our previous analysis that a TQC cannot trap massless DFs. The spatial patterns of these states were imaged by taking d*I*/d*V* maps in the energy range from −400 to 500 meV with a 25-meV interval (see fig. S2). Figure 2 shows the d*I*/d*V* maps at some representative energies that capture the main feature of trapping behaviors of TSS. The regular patterns can be seen below −250 meV or above −175 meV, and no pattern can be seen in between (except a bulk state–related pattern at −240 meV, which can be seen in Fig. 1B and more clearly in the Discussion). The patterns in the energy window from −175 to −100 meV are relatively weak and get much stronger above −75 meV.

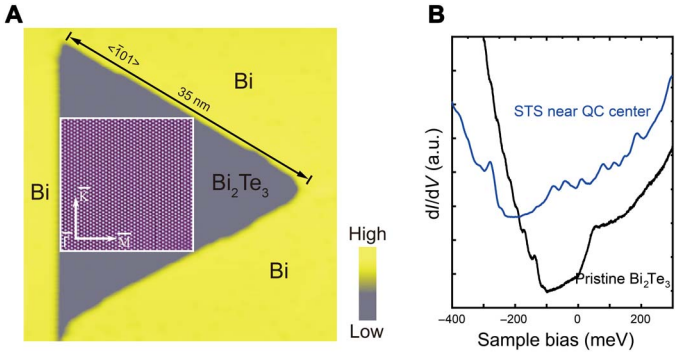

Fig. 1. Surface topography of the 0.9 BL Bi film on Bi_2Te_3 films. (**A**) Typical equilateral triangular Bi_2Te_3 vacancy island surrounded by Bi BLs (brighter regions) (42 nm × 42 nm, tunneling condition: 0.5 V, 0.1 nA). The Bi BL was grown on the Bi_2Te_3 film by MBE. The thickness of the Bi_2Te_3 film is 15 quintuple layers. The atomic resolution image in the white square shows the defect-free Te-terminated Bi_2Te_3 (16 nm × 16 nm, −0.4 V, 0.4 nA). $\bar{\Gamma}-\bar{M}$ and $\bar{\Gamma}-\bar{K}$ in the momentum space are shown to indicate their alignment with the TQC edges. (**B**) Typical d*I*/d*V* spectra taken near the TQC center in (A) (upper curve) and on pristine Bi_2Te_3 (lower curve). The curves are vertically offset for clarity. a.u., arbitrary units.

Modeling of the interference patterns

A simple particle-in-a-box model (*23*) is used and diagrammed in Fig. 3 (A and B) to simulate the above patterns and to elucidate the exact nature of these trapped states as well as the TSS selection rules in such a TQC. Provided the reflections are appreciable, an electron in a TQC with a side length of L can be possibly trapped by successive reflections at the triangular barrier walls, generating six wave vectors—$\mathbf{k}_1$, $\mathbf{k}_2$, $\mathbf{k}_3$, $\mathbf{k}_4$, $\mathbf{k}_5$, and $\mathbf{k}_6$—which have the c_{3v} symmetry and are related to each other by in-plane 120° rotations and by reflections with respect to $\bar{\Gamma}-\bar{K}$ (Fig. 3, B and C). Taking the coordinates as shown in Fig. 3A and by imposing the boundary condition, these superpositions of momentum states are then quantized, such as $\mathbf{k}_1 = \left(\frac{2\pi}{3L}(2n-m), \frac{2\pi}{\sqrt{3}L}m\right)$

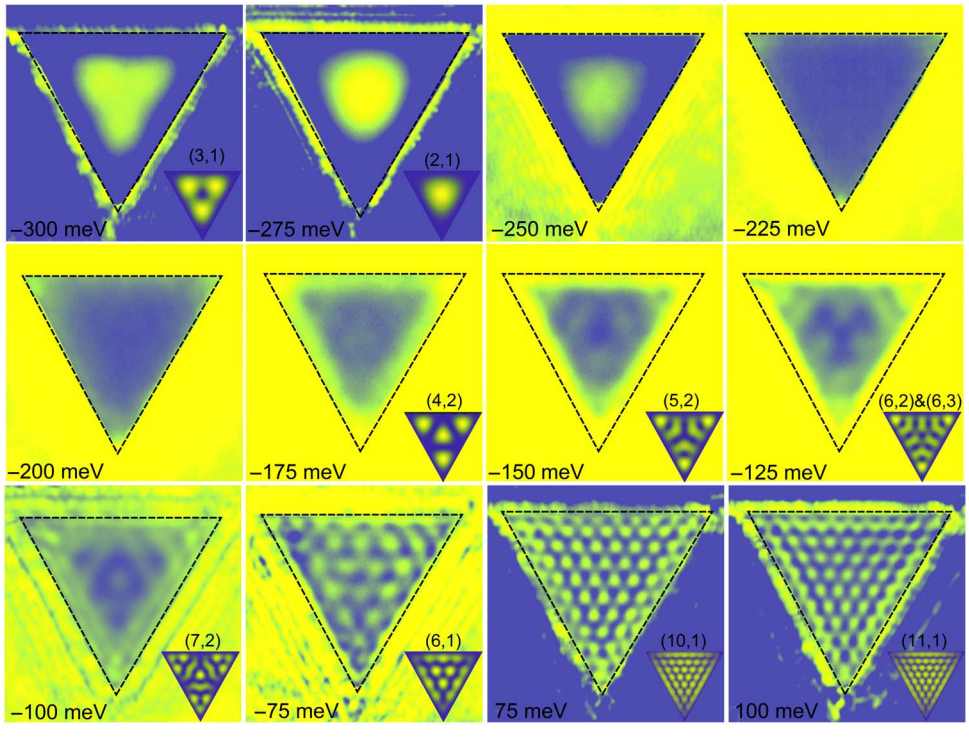

Fig. 2. Quasi-bound states in a TQC (*L* = 35 nm). Spatial d*I*/d*V* maps of TQC in Fig. 1A (42 nm × 42 nm) at different energies (−300, −275, −250, −225, −200, −175, −150, −125, −100, −75, 75, and 100 meV) (see fig. S2 for more images at other energies). The dashed triangles are guides for the eye, indicating the position of triangular barriers. The inset in each image is the simulated pattern of a certain index, which matches the interference pattern best. In this simulation, the spinor part of the wave function is omitted, which may only affect the overall intensity and does not contribute to the spatial variation of the pattern.

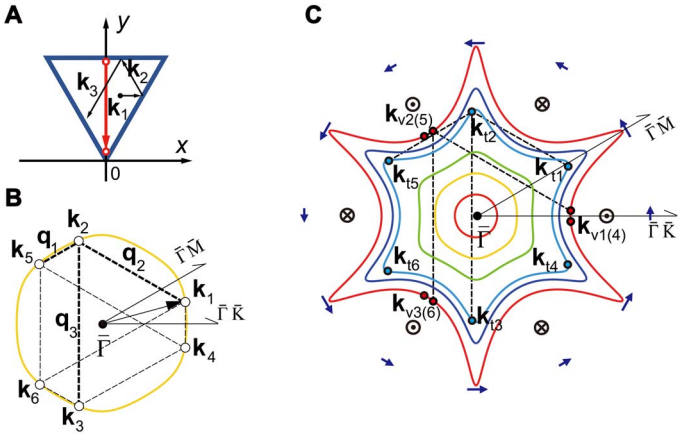

Fig. 3. Scattering process of possible quasi-bound surface states in Bi_2Te_3 in a TQC. (**A**) Schematic diagram of the scattering process of surface states inside the TQC. The thick (red) arrow indicates where the spatially dependent d*I*/d*V* spectra in Fig. 4 were taken. (**B** and **C**) Scattering process shown on the energy-dependent CECs of TSS with a strong warping effect. The dashed lines in (B) indicate the possible scattering vectors between wave vectors $\mathbf{k}_1$ to $\mathbf{k}_6$. $\mathbf{q}_1$, $\mathbf{q}_2$, and $\mathbf{q}_3$ denote three inequivalent reflections. $\mathbf{k}_{ti}$ and $\mathbf{k}_{vi}$ are the wave vectors close to the tip and valley positions on the warped CECs, respectively. At high energies, the CECs are labeled with a spin texture exclusively for TSS with a strong warping term. Note that because of the warping effect, the spin-momentum helicity deviates from those at low energies, acquiring an out-of-plane spin component in the valley positions, as indicated by the crosses and dots in (C). The arrows with different lengths show the in-plane spin components with different magnitudes.

with a magnitude of $k_{nm} = \frac{4\pi}{3L}\sqrt{n^2 + m^2 - nm}$. Therefore, by matching the interference patterns at specific energies, a series of (E_{nm}, k_{nm}) states can be obtained to form the (n, m) quasi-bound states of TSS in the TQC. Because of the degeneracy caused by symmetry, only the states of $n \geq 2m$ are considered, where n, m are positive integers. Note that the defect-free condition is indispensable in this work. Otherwise, the existence of point scatterers will invalidate the above model.

The simulated eigenmodes are shown in the insets of Fig. 2, which fit the interference patterns best at different energies. The patterns at and below −250 meV are found (see Discussion) to be caused by the band bending of the bulk states, except those at −275 and −300 meV, which are attributed to the (2, 1) and (3, 1) states, respectively. The patterns from −175 to −100 meV all have higher m indexes ($m \geq 2$) but are relatively weak, much weaker than the spectral intensity of the Bi BL, especially the one at −175 meV, which is nearly indiscernible. At energies above −75 meV, the interference patterns get stronger and switch to low m indexes ($m = 1$).

In the diagram of Fig. 3C, the vector series corresponding to low or high m–indexed states are indicated on the energy-dependent CECs of TSS in Bi_2Te_3, as well as the complicated spin texture due to the strong hexagonal warping. For the (n, 1) states, the vectors $\mathbf{k}_{vi}$ are close to valley positions in $\bar{\Gamma} - \bar{K}$ directions on the warped CECs (the wave vectors for $m = 0$ states are exactly along $\bar{\Gamma} - \bar{K}$ directions, but the corresponding wave functions are zero inside the TQC). For states with higher m indexes, the vectors $\mathbf{k}_{ti}$ are close to tip positions in $\bar{\Gamma} - \bar{M}$ directions on the CECs. Note that vectors of the ($n = 2m$, m) states are exactly along $\bar{\Gamma} - \bar{M}$ directions. Thus, the scattering process of the surface states inside the TQC reveals a strong energy-dependent trapping of TSS, selecting momenta in different directions on the CECs, which, due to the strong warping effect, have quite different magnitudes and spin orientations (*19*).

DISCUSSION

The identification of trapped states below the highest valence subband

Figure 4A provides the spatially resolved energy levels of trapped states by taking the d*I*/d*V* spectra along the line across the TQC (thick arrow in Fig. 3A). E_c (−75 meV) denotes the conduction band minimum as identified by the d*I*/d*V* spectra (Fig. 1B). By using the pattern in Fig. 4A, the correction of the energies of the trapped states can be made. In addition, two trapped surface states (2, 1) and (3, 1) are identified. The spots at or below −240 meV, which correspond to the peaks in the d*I*/d*V* spectra of different sized TQCs (35 and 17 nm; see fig. S3), reflect the bulk valence subbands. The highest valence subband (denoted as E_v ~−240 meV) also shows as a peak (~−110 meV) in the d*I*/d*V* spectrum on the pristine Bi_2Te_3 film (Fig. 1B) but with an energy shift caused by different doping. These bulk-related patterns are identified to be the density variation of valence band states caused by band bending in the lateral direction near the steps; as noted above, the Bi BL has a strong electron-doping effect on Bi_2Te_3. The (2, 1) state centered at −280 meV in Fig. 4A, corresponding to the pattern at −275 meV, obeys a sinusoidally spatial intensity distribution, which is in contrast to other patterns below E_v. The (3, 1) pattern at ~−300 meV (~−320 meV after correction) does not have a node in the TQC center because of its weak intensity and the relatively stronger density variation of bulk states caused by band bending.

Seven different energy regions in the band structure of Bi_2Te_3

Thus, by a careful investigation of Fig. 4 (A and B), as well as the interference patterns at different energies (Fig. 2 and fig. S2), seven energy regions with distinct trapping behaviors or interference patterns are identified. The first region is below −320 meV, in which, except for the patterns caused by band bending, no trapped state can be observed. The second region is from −320 meV to E_v. Besides the patterns coming from the band-bending effect, two trapped states, (3, 1) at −320 meV and (2, 1) at −280 meV, are found. The (3, 1) state has a clover shape that cannot be explained by the band-bending effect. The pronounced peak of the (2, 1) state occurs in the d*I*/d*V* spectra of the TQC (L = 35 nm) but does not appear in that of a smaller TQC (L = 17 nm; see fig. S3) and that of the pristine film, indicating its trapped nature. The third region is from E_v to E_w (175 meV), in which no pattern appears (Figs. 2 and 4B). Here, E_w denotes approximately the energy above which the CEC of TSS becomes concave. The fourth region is from E_w to E_c (−75 meV), in which there are very weak patterns (Fig. 2). These weak patterns all match with the states of (n, $m \geq 2$). The fifth region is from E_c to 75 meV. In this region, the patterns are stronger but seem mixed such that there are no clear spots or nodes in the spatial map of energy levels (Fig. 4B), although the dominating contribution comes from the (n, 1) modes. The pattern mixing is possible because of the level broadening caused by the finite lifetime of the trapped states and the unequal spaced energy levels of (n, m) states (some states with different n and different m may be very close). This means that the trapping probabilities of different channels are competing in such an energy range. The sixth region is from 75 to 400 meV, in which strong ($n \geq 10$, 1) patterns are obvious at a glance. The indexing of trapped states can be double-checked by the symmetry of the (n, m) states. This can be done by noting that ($3i + 2$, $3j + 1$) and ($3i + 1$, $3j + 2$) states (i and j are nonnegative integers) have an antinode at the center of the TQC (dashed line in Fig. 4A). The last region is above 400 meV, where there are no more clear patterns. Note that the absence of trapped states in regions 1 and 7 is a result of the finite energy range of TSS.

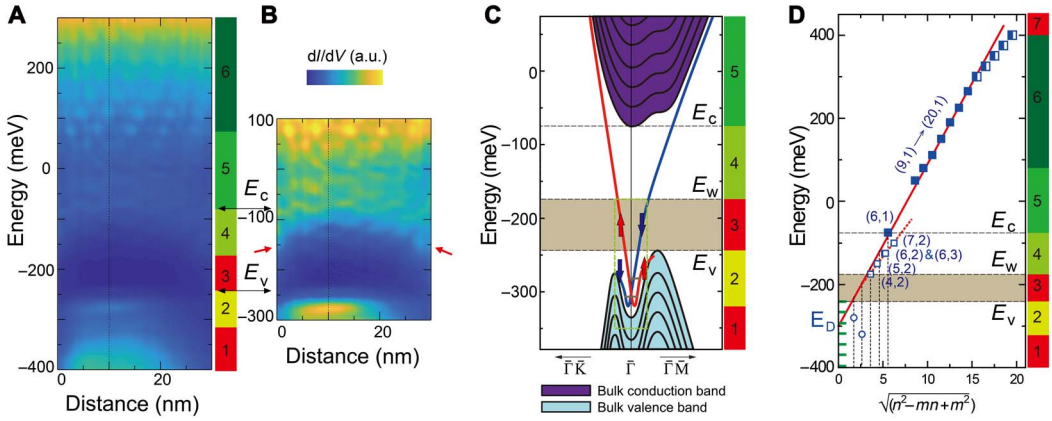

Fig. 4. Spatially dependent energy levels inside the TQC (*L* = 35 nm) and the derived spectrum of trapped TSS. (**A**) Bias and spatially dependent d*I*/d*V* spectra along the line in Fig. 3A (tunneling condition: 0.2 V, 0.2 nA). The dashed line indicates the center position of the TQC. The sidebar indicates the energy regions as described in the main text having different trapping behaviors. (**B**) Blow-up maps from −300 to 100 meV. The red arrows indicate the localized states near the barriers. (**C**) Schematic of the band structure of Bi_2Te_3 thin films. The two short lines indicate the states (2, 1) and (3, 1) (see fig. S6 for details of the green dashed region). (**D**) Spectrum (E_{nm}, k'_{nm}) of trapped TSS, where $k'_{nm} = \frac{3L}{4\pi}k_{nm}$. The half-filled squares [states ($n \geq 16$, 1)] are obtained by counting the nodes in the d*I*/d*V* maps shown in fig. S2. The red solid and dashed lines are the linear fitting to the states ($n \geq 6$, 1) (filled squares) and the states (n, $m \geq 2$) (hollow squares), respectively. The equal-spaced short lines between −400 and − 240 meV indicate the peak positions in the d*I*/d*V* spectrum coming from the bulk valence subbands of the Bi_2Te_3 film. The dashed vertical lines indicate the positions of k'_{n1}, where n ranges from 2 to 6. The gray regions in (C) and (D) denote the forbidden region for the trapping of TSS.

Detailed nature of the trapped TSS in four regions (6, 5, 4, and 2)

On the basis of the above observation and discussion, the schematic band structure of our Bi_2Te_3 thin film is shown in Fig. 4C. Figure 4D gives a summary of the indexed states trapped by the TQC (L = 35 nm). The energies of the trapped states are all corrected by Fig. 4A, except those above 250 meV (half-filled squares). Here, we may focus on the details of the abovementioned trapping behaviors (in regions 6, 5, 4, and 2). For the ($n \geq 6$, 1) states (regions 6 and 5; filled squares in Fig. 4D), the vectors $\mathbf{k}_{vi}$ are close to valley positions in $\bar{\Gamma} - \bar{K}$ directions on the warped CECs (Fig. 3C). Thus, the derived dispersion by fitting (red solid line) gives the Fermi velocity of Bi_2Te_3 thin films in the $\bar{\Gamma} - \bar{K}$ direction, $v_{F1} \sim 4.9 \times 10^5$ m/s, consistent with the result from step-edge scattering (*4*). At higher energies, the step-edge scattering, which may have different scattering vectors, starts to dominate the interference pattern near the edges (above 200 meV in fig. S2), resulting in the inaccuracy of counting the nodes of the trapped modes (the deviation of half-filled squares from the linear dispersion of TSS). In addition, the energy correction by Fig. 4A is impossible for states above 250 meV. The extrapolation of the fitting yields a Dirac energy of ~−300 meV, in excellent agreement with our d*I*/d*V* spectra (*21*). These trapped ($n \geq 6$, 1) states are no doubt from TSS because, for the 35-nm TQC, the (6, 1) state instead of the ground state (2, 1) of the conduction band parabola lies close to the conduction band minimum. It is also not likely that a Bi overlayer can trap the bulk states that extend across the whole thickness of the film.

For the higher m–indexed (n, $m \geq 2$) states (region 4, hollow squares from −175 to −100 meV in Fig. 4D), the vectors $\mathbf{k}_{ti}$ are close to tip positions in $\bar{\Gamma} - \bar{M}$ directions on CECs (Fig. 3C). These in-gap high-m states are exclusively from TSS. The slower Fermi velocity $v_{F2} \sim 3.6 \times 10^5$ m/s is in agreement with a sudden decrease of the slope of the TSS band along $\bar{\Gamma} - \bar{M}$ directions above E_w (*6*). Note that the trapping of these high-m states involves scattering between states on the CEC that are nearly time-reversal symmetric (TRS), especially for the ($n = 2m$, m) states. This situation is different from the interference pattern of TSS scattered by a single line defect (*4*, *24*, *25*), where the nesting vector ($\mathbf{q}_2$) connecting, for example, $\mathbf{k}_{t2}$ and $\mathbf{k}_{t3}$ induces a strong interference pattern. In the TQC case, the absence of scattering vector $\mathbf{q}_3$ ($\mathbf{q}_3$ connects two nearly TRS counterparts) will render the trapping states (n, $m \geq 2$), especially the ($n = 2m$, m) states, of TSS impossible even in the presence of strong reflections $\mathbf{q}_2$. There must be a TRS-breaking mechanism for the appearance of these high m–indexed states.

The (2, 1) and (3, 1) states below E_v (region 2) are also from TSS by using the argument for the states above E_c and also by noting that there is only one (2, 1) state despite the multiple valence subbands. However, the appearance of the (2, 1) state, especially its strong intensity, seems like a puzzle based on the arguments above, contradicting TRS.

The mechanism of three kinds of trapping behaviors

Our interpretation of these three kinds of trapping (in regions 2, 4, 5, and 6) behaviors is as follows. First, the Dirac energy is buried well below E_v. This makes the trapping of TSS below E_v (region 2) possible because there may exist two Fermi pockets with inverted spin textures similar to the antimony case (*6*, *18*), especially for the (2, 1) state, as shown in fig. S6, where the backscattering is no longer forbidden. The deviation of k'_{21} from the TSS dispersion (Fig. 4D) results from the fact that the trapping now involves wave vectors from multiple Fermi surfaces. This scenario supports the situation that the Dirac point lies below the (2, 1) state, in agreement with our observation. The absence of the (2, 1) state for the smaller TQC (L = 17 nm; fig. S4) is reasonable because its energy may lie in the energy region where trapping is impossible (region 3).

The other two trapping behaviors (in regions 4, 5, and 6) are found to be caused by the strong hexagonal warping in Bi_2Te_3, which leads to heavily deformed CECs and modified spin textures of TSS band (*19*). The energy-dependent CECs evolve from a circle near the Dirac point to a hexagon and then to a snowflake (*6*). In the case of a concave CEC above a certain energy, there may exist spin-polarized local modes along a line defect extended in the $\bar{\Gamma} - \bar{K}$ direction (*26*). The existence of bound states near the step edge on Bi_2Te_3 has been reported before (*27*). Thus, the occurrence of trapped states in the forbidden gap (region 4) may be ascribed to the simultaneous appearance

of localized states along the barriers (Figs. 2 and 4B or fig. S5). These localized states are even stronger in intensity than the interference patterns inside the TQC and may act as a magnetic barrier that opens the channel of nearly normal reflections responsible for the trapping of (n, $m \geq 2$) states. Nonetheless, the patterns of ($2m$, m) states should still be absent because of the orthogonality of scattering vectors in the spinor basis. The TRS counterparts simply do not interfere (*28*). These (n, $m \geq 2$) patterns are all very weak, especially the almost indiscernible (4, 2) pattern at −175 meV, as shown in our experiment. The pattern at −125 meV (Fig. 2) has contributions from the (6, 2) and (6, 3) modes but with an intensity ratio of about 2:1, although these two modes are nearly degenerated (k_{62} and k_{63} are close). Their appearance, although very weak, may originate from the nonideal shape of the TQCs in some sense, which may result in a nonperfect alignment between the TQC edges and the $\bar{\Gamma} - \bar{K}$ directions. The trapping of the (2, 1) state below E_v involves backscattering between electronic states with the same spin direction, which is different from this scenario and explains the strong intensity of the (2, 1) pattern at −275 meV.

Furthermore, the complexity of the spin texture (diagrammed in Fig. 3C) due to the strong hexagonal warping (*19*) may account for the appearance and the growing intensity of the ($n \geq 6$, 1) states with energy. In the modified spin texture, the spin polarization near the $\bar{\Gamma} - \bar{K}$ directions is mostly affected, with the spin gradually canting toward the out-of-plane direction. Thus, the reflections between these valley points ($\mathbf{k}_{vi}$) increase with energy (*13*), modifying drastically the reflectivity incident angle relation compared to the case of TSS with a simple spin-momentum texture. Note that the wave vectors of the ($n \geq 6$, 1) states are not perfectly along $\bar{\Gamma} - \bar{K}$ directions. The trapping of these states is composed of these intervalley reflections ($\mathbf{q}_2$ and $\mathbf{q}_3$) and intravalley ones ($\mathbf{q}_1$, grazing angles). The larger z component conformity of spins between the scattering wave vectors also makes the interference pattern stronger with energy (*13*). This explains the existence of a transit region 5 [from (n, $m \geq 2$) to (n, 1) domination], where the interference patterns are complicated. The region 5 in our case is from E_c to 75 meV. Below E_c, the (n, 1) states are missing, such as the (4, 1) and (5, 1) states. Above 75 meV, only the (n, 1) states are visible in the dI/dV maps. A previous experiment (*24*) also observed an anomaly at some energy above E_c in the interference patterns along the step edge. We argue this anomaly by the change of phase shift at the boundary with energy. This can be seen more obviously by investigation of the patterns (near the edges) of 50, 75, and 100 meV (fig. S7), which indicates a phase shift change from 0 to π above E_c. This implies that the dominant scattering process responsible for the trapping of TSS changes above E_c, in accordance with the switch of trapped modes from (n, $m \geq 2$) to (n,1). The deviation of the phase shift from π below 100 meV results in an underestimation of k_{nm}, which explains the slight deviation of states (9, 1) and (10, 1) from the linear fitting quite well (Fig. 4D). Furthermore, the trapping of TSS above E_c via bulk states is unlikely, because at low temperatures (~ 4 K) the phonon-assisted inelastic scattering between TSS and the bulk states is totally suppressed. They behave more like two independent electron systems that are weakly coupled even at room temperature, with a time scale of several picoseconds (*29*, *30*).

Despite all the abovementioned reflectivity-improving mechanisms that help to trap the DFs in TIs, the lifetime of the trapped states is still limited. The typical lifetime estimated from the peak widths (from 20 to 40 meV) ranges from 20 to 40 fs, which corresponds roughly to the reflectivity of TSS at the TQC edges from ~0.12 to ~0.35 (see fig. S8 for details). Here, only the states (n, 1) are discussed because the high-m states are too weak. The relatively low reflectivity indicates the high transmission of TSS at the TQC edges.

CONCLUSIONS

To conclude, despite the promised transparency of TQCs for TSS, three situations to trap the TSS are directly visualized in our work. One is the presence of double Fermi surfaces having opposite spin textures. For Bi_2Te_3, this region lies below the bulk valence band maximum. The other two take advantage of the strong hexagonal warping of TSS in Bi_2Te_3, which leads to the existence of possibly magnetic bound states and a more complicated spin texture. While the former opens the forbidden backscattering channels that facilitate the trapping of the high m–indexed (n, $m \geq 2$) states of TQCs, the latter favors the trapping of the (n, 1) states, selecting the states near the tips ($\mathbf{k}_{ti}$) and those close to the valleys ($\mathbf{k}_{vi}$) on the CEC, respectively. In the situation where all the aforementioned conditions are absent, the TQCs are completely transparent for the TSS, in agreement with the argument presented at the beginning. This region in Bi_2Te_3 is from E_v to E_v+85 meV, where the CECs of TSS are supposed to be convex, constituting a truly forbidden region to trap the TSS. Note that the (3, 1) and (4, 1) states (Fig. 4D) above the Dirac point are missing. Similar experiments can be conducted on TIs without strong hexagonal warping (Bi_2Se_3 or Sb_2Te_3), which may have different trapping behaviors and may further validate our interpretation of current results. Thus, our findings elucidate the trapping and the detrapping behaviors of TSS in the presence of complicated CEC geometry and spin textures, giving insight into the manipulation of TSS, which is especially intriguing owing to their massless, relativistic and spin 1/2 DF nature.

MATERIALS AND METHODS

MBE growth and scanning tunneling microscopic characterizations

The main experiments were performed in ultrahigh vacuum (base pressure, $\leq 1.0 \times 10^{-10}$ torr) using a commercial molecular beam epitaxy (MBE)–low temperature (LT) scanning tunneling microscopic (STM) combined system (Unisoku). Bi(111) BL films were heteroepitaxially grown on pristine Bi_2Te_3 films (thickness, ~15 quintuple layers) supported by graphitized SiC substrates. After growth, the samples were immediately transferred into in situ LT-STM so that the vacancy island shape could be frozen at 4.36 K to avoid Bi migration. The mechanically sharpened PtIr tips were used for STM after calibration on standard Pb/Si(111). Point scanning tunneling spectrum (STS or dI/dV) was performed with feedback loop open (lock-in bias modulation: 1 to 3 mV_{rms} at 987.5 Hz), and dI/dV maps were obtained simultaneously with constant current images (8 to 10 mV_{rms} at 2997 Hz). All the energies are shown with respect to the Fermi level (E_F). The STM images were processed using WSxM software.

SUPPLEMENTARY MATERIALS

Supplementary material for this article is available at http://advances.sciencemag.org/cgi/content/full/5/5/eaaw3988/DC1

Fig. S1. Band structure of Bi/Bi_2Te_3 on (111) surface.
Fig. S2. Successive dI/dV maps of the TQC (35 nm) at energies with an interval of 25 meV.
Fig. S3. dI/dV spectra on TQCs of different sizes.
Fig. S4. dI/dV maps on a smaller TQC (17 nm).
Fig. S5. dI/dV spectra of Fig. 4A in the line plot form.
Fig. S6. A zoom-in view of the schematic band structure in Fig. 4C.

Fig. S7. Section profiles of patterns at 50, 75, and 100 meV along the lines indicated in fig. S2.
Fig. S8. A particular situation adopted to give a rough estimation of the trapped states' lifetime in which the path of the electron in a TQC roughly follows a regular pattern.

REFERENCES AND NOTES

1. M. Z. Hasan, C. L. Kane, *Colloquium*: Topological insulators. *Rev. Mod. Phys.* **82**, 3045–3067 (2010).
2. X.-L. Qi, S.-C. Zhang, Topological insulators and superconductors. *Rev. Mod. Phys.* **83**, 1057–1110 (2011).
3. J. Seo, P. Roushan, H. Beidenkopf, Y. S. Hor, R. J. Cava, A. Yazdani, Transmission of topological surface states through surface barriers. *Nature* **466**, 343–346 (2010).
4. T. Zhang, P. Cheng, X. Chen, J.-F. Jia, X. Ma, K. He, L. Wang, H. Zhang, X. Dai, Z. Fang, X. Xie, Q.-K. Xue, Experimental demonstration of topological surface states protected by time-reversal symmetry. *Phys. Rev. Lett.* **103**, 266803 (2009).
5. P. Roushan, J. Seo, C. V. Parker, Y. S. Hor, D. Hsieh, D. Qian, A. Richardella, M. Z. Hasan, R. J. Cava, A. Yazdani, Topological surface states protected from backscattering by chiral spin texture. *Nature* **460**, 1106–1109 (2009).
6. Y. L. Chen, J. G. Analytis, J.-H. Chu, Z. K. Liu, S.-K. Mo, X. L. Qi, H. J. Zhang, D. H. Lu, X. Dai, Z. Fang, S. C. Zhang, I. R. Fisher, Z. Hussain, Z.-X. Shen, Experimental realization of a three-dimensional topological insulator, Bi_2Te_3. *Science* **325**, 178–181 (2009).
7. Y. Xia, D. Qian, D. Hsieh, L. Wray, A. Pal, H. Lin, A. Bansil, D. Grauer, Y. S. Hor, R. J. Cava, M. Z. Hasan, Observation of a large-gap topological-insulator class with a single Dirac cone on the surface. *Nat. Phys.* **5**, 398–402 (2009).
8. H. Zhang, C.-X. Liu, X.-L. Qi, X. Dai, Z. Fang, S.-C. Zhang, Topological insulators in Bi_2Se_3, Bi_2Te_3 and Sb_2Te_3 with a single Dirac cone on the surface. *Nat. Phys.* **5**, 438–442 (2009).
9. L. Fu, C. L. Kane, E. J. Mele, Topological insulators in three dimensions. *Phys. Rev. Lett.* **98**, 106803 (2007).
10. M. F. Crommie, C. P. Lutz, D. M. Eigler, Imaging standing waves in a two-dimensional electron gas. *Nature* **363**, 524–527 (1993).
11. M. I. Katsnelson, K. S. Novoselov, A. K. Geim, Chiral tunnelling and the Klein paradox in graphene. *Nat. Phys.* **2**, 620–625 (2006).
12. Z.-G. Fu, P. Zhang, M. Chen, Z. Wang, F.-W. Zheng, H.-Q. Lin, Anisotropic Fabry-Pérot resonant states confined within nano-steps on the topological insulator surface. *Sci. Rep.* **4**, 5544 (2014).
13. W.-C. Lee, C. Wu, D. P. Arovas, S.-C. Zhang, Quasiparticle interference on the surface of the topological insulator Bi_2Te_3. *Phys. Rev. B* **80**, 245439 (2009).
14. S.-Y. Xu, Y. Xia, L. A. Wray, S. Jia, F. Meier, J. H. Dil, J. Osterwalder, B. Slomski, A. Bansil, H. Lin, R. J. Cava, M. Z. Hasan, Topological phase transition and texture inversion in a tunable topological insulator. *Science* **332**, 560–564 (2011).
15. Y. Zhao, J. Wyrick, F. D. Natterer, J. F. Rodriguez-Nieva, C. Lewandowski, K. Watanabe, T. Taniguchi, L. S. Levitov, N. B. Zhitenev, J. A. Stroscio, Creating and probing electron whispering-gallery modes in graphene. *Science* **348**, 672–675 (2015).
16. J. Lee, D. Wong, J. Velasco Jr., J. F. Rodriguez-Nieva, S. Kahn, H.-Z. Tsai, T. Taniguchi, K. Watanabe, A. Zettl, F. Wang, L. S. Levitov, M. F. Crommie, Imaging electrostatically confined Dirac fermions in graphene quantum dots. *Nat. Phys.* **12**, 1032–1036 (2016).
17. C. Gutiérrez, L. Brown, C.-J. Kim, J. Park, A. N. Pasupathy, Klein tunnelling and electron trapping in nanometre-scale graphene quantum dots. *Nat. Phys.* **12**, 1069–1075 (2016).
18. D. Hsieh, Y. Xia, L. Wray, D. Qian, A. Pal, J. H. Dil, J. Osterwalder, F. Meier, G. Bihlmayer, C. L. Kane, Y. S. Hor, R. J. Cava, M. Z. Hasan, Observation of unconventional quantum spin textures in topological insulators. *Science* **323**, 919–922 (2009).
19. L. Fu, Hexagonal warping effects in the surface states of the topological insulator Bi_2Te_3. *Phys. Rev. Lett.* **103**, 266801 (2009).
20. K. Kuroda, M. Arita, K. Miyamoto, M. Ye, J. Jiang, A. Kimura, E. E. Krasovskii, E. V. Chulkov, H. Iwasawa, T. Okuda, K. Shimada, Y. Ueda, H. Namatame, M. Taniguchi, Hexagonally deformed fermi surface of the 3D topological insulator Bi_2Se_3. *Phys. Rev. Lett.* **105**, 076802 (2010).
21. M. Chen, J.-P. Peng, H.-M. Zhang, L.-L. Wang, K. He, X.-C. Ma, Q.-K. Xue, Molecular beam epitaxy of bilayer Bi(111) films on topological insulator Bi_2Te_3: A scanning tunneling microscopy study. *Appl. Phys. Lett.* **101**, 081603 (2012).
22. T. Hirahara, G. Bihlmayer, Y. Sakamoto, M. Yamada, H. Miyazaki, S.-i. Kimura, S. Blügel, S. Hasegawa, Interfacing 2D and 3D topological insulators: Bi(111) bilayer on Bi_2Te_3. *Phys. Rev. Lett.* **107**, 166801 (2011).
23. T. Kumagai, A. Tamura, Analysis of scanning tunneling microscopy images and scanning tunneling spectrum of electrons confined in equilateral triangular quantum corrals. *J. Phys. Soc. Japan* **77**, 014601 (2007).
24. Z. Alpichshev, J. G. Analytis, J. H. Chu, I. R. Fisher, Y. L. Chen, Z. X. Shen, A. Fang, A. Kapitulnik, STM imaging of electronic waves on the surface of Bi_2Te_3: Topologically protected surface states and hexagonal warping effects. *Phys. Rev. Lett.* **104**, 016401 (2010).
25. J. Wang, W. Li, P. Cheng, C. Song, T. Zhang, P. Deng, X. Chen, X. Ma, K. He, J.-F. Jia, Q.-K. Xue, B.-F. Zhu, Power-law decay of standing waves on the surface of topological insulators. *Phys. Rev. B* **84**, 235447 (2011).
26. J. An, C. S. Ting, Surface states scattering from a step defect in the topological insulator Bi_2Te_3. *Phys. Rev. B* **86**, 165313 (2012).
27. Z. Alpichshev, J. G. Analytis, J.-H. Chu, I. R. Fisher, A. Kapitulnik, STM imaging of a bound state along a step on the surface of the topological insulator Bi_2Te_3. *Phys. Rev. B* **84**, 041104 (2011).
28. J. I. Pascual, G. Bihlmayer, Y. M. Koroteev, H. P. Rust, G. Ceballos, M. Hansmann, K. Horn, E. V. Chulkov, S. Blügel, P. M. Echenique, P. Hofmann, Role of spin in quasiparticle interference. *Phys. Rev. Lett.* **93**, 196802 (2004).
29. Y. H. Wang, D. Hsieh, E. J. Sie, H. Steinberg, D. R. Gardner, Y. S. Lee, P. Jarillo-Herrero, N. Gedik, Measurement of intrinsic dirac fermion cooling on the surface of the topological insulator Bi_2Se_3 using time-resolved and angle-resolved photoemission spectroscopy. *Phys. Rev. Lett.* **109**, 127401 (2012).
30. C. Cacho, A. Crepaldi, M. Battiato, J. Braun, F. Cilento, M. Zacchigna, M. C. Richter, O. Heckmann, E. Springate, Y. Liu, S. S. Dhesi, H. Berger, P. Bugnon, K. Held, M. Grioni, H. Ebert, K. Hricovini, J. Minár, F. Parmigiani, Momentum-resolved spin dynamics of bulk and surface excited states in the topological insulator Bi_2Se_3. *Phys. Rev. Lett.* **114**, 097401 (2015).

Acknowledgments: We thank C.-L. Song, S.-Q. Shen, Y.-Y. Wang, Z.-X. Gong, and P.-Z. Tang for helpful discussions. **Funding:** This work was supported by the National Science Foundation, the Ministry of Science and Technology of China, and, in part, the Beijing Advanced Innovation Center for Future Chip. Y.-P.J. acknowledges support from the National Thousand Young Talents Program. C.-Z.C. acknowledges support from Alfred P. Sloan Research Fellowship and ARO Young Investigator Program Award (no. W911NF1810198). **Author contributions:** M.C., X.-C.M., and Q.-K.X. conceived and designed the experiments. M.C., J.P., and H.Z. carried out MBE growth and STM measurements. C.-Z.C. and X.F. carried out the angle-resolved photoemission spectroscopy measurements. L.W. and K.H. assisted the experiments. Z.F., F.Z., and P.Z. did the band structure calculation for the heterostructure. Y.-P.J., M.C., and X.-C.M. carried out the data analyses and interpretations. Y.-P.J., M.C., and X.-C.M. wrote the manuscript. **Competing interests:** The authors declare that they have no competing interests. **Data and materials availability:** All data needed to evaluate the conclusions in the paper are present in the paper and/or the Supplementary Materials. Additional data related to this paper may be requested from the authors. Correspondence and requests for materials should be addressed to Y.-P.J., X.-C.M., and Q.-K.X.

Submitted 17 December 2018
Accepted 9 April 2019
Published 17 May 2019
10.1126/sciadv.aaw3988

Citation: M. Chen, Y.-P. Jiang, J. Peng, H. Zhang, C.-Z. Chang, X. Feng, Z. Fu, F. Zheng, P. Zhang, L. Wang, K. He, X.-C. Ma, Q.-K. Xue, Selective trapping of hexagonally warped topological surface states in a triangular quantum corral. *Sci. Adv.* **5**, eaaw3988 (2019).

Selective trapping of hexagonally warped topological surface states in a triangular quantum corral

Mu Chen, Ye-Ping Jiang, Junping Peng, Huimin Zhang, Cui-Zu Chang, Xiao Feng, Zhenguo Fu, Fawei Zheng, Ping Zhang, Lili Wang, Ke He, Xu-Cun Ma and Qi-Kun Xue

Sci Adv **5** (5), eaaw3988.
DOI: 10.1126/sciadv.aaw3988